Tungsten (2024) 6:367–381
https://doi.org/10.1007/s42864-023-00241-1

Tungsten
www.springer.com/42864

ORIGINAL PAPER

Nickel sulfate solution fluoride separation with hydrous zirconium oxide

Elbert M. Nigri[1] · Ummul K. Sultana[2] · André L. A. Santos[1] · James W. Vaughan[2] · Sônia D. F. Rocha[1]

Received: 2 June 2023 / Revised: 22 June 2023 / Accepted: 30 June 2023 / Published online: 10 October 2023

Abstract
Fluoride is an impurity in nickel sulfate production, which is required for electric vehicle batteries. Hydrous zirconium oxide (HZO) was evaluated for removing fluoride from nickel sulfate solution. Maximum fluoride removal occurred at pH value 4 and optimal pH value is 4–5, considering Zr solubility. Fluoride availability decreases with pH due to hydrogen fluoride and zirconium fluoride aqueous species. Fluoride removal is initially rapid, with 50 wt.% removal in 7 min, followed by slow removal up to 68 wt.% after 72 h and follows second order rate kinetics. Fluoride removal was dominated by an ion exchange mechanism and resulting Zr–F bonds were observed using Fourier-transform infrared spectroscopy. The presence of nickel sulfate decreased loading capacity compared to a salt-free solution. HZO maintained adsorption capacity through five cycles of loading and regeneration.

Keywords Hydrous zirconium oxide · Nickel sulfate · Fluoride · Adsorption · Anion exchange

1 Introduction

With the exhaustion of large deposits of high-grade nickel sulfides, the processing of nickel laterite ores, also containing cobalt and manganese, has become the main source of this metal [1–4]. In the comparatively energy intense pyrometallurgical processes to generate ferronickel or nickel pig iron, cobalt is generally not recovered [5]. Both nickel and cobalt are increasingly in demand for their key role in the cathode active material of rechargeable lithium-ion batteries (LIB) used in electric vehicles. Hydrometallurgical processing is preferred for relatively low-grade ores containing significant cobalt value and hydrometallurgical approaches are now common for lithium-ion battery recycling.

In primary production, after leaching the ore with sulfuric acid, an intermediate precipitation stage is usually part of the purification of nickel and cobalt from the liquor producing a mixed nickel–cobalt hydroxide precipitate (MHP) which is an intermediate product [6, 7]. MHP contains relatively large amounts of impurities due to the low selectivity in the hydroxide precipitation process compared with sulfide precipitation [4, 6–8]. Ordinarily, magnesia, which is commonly used for precipitating MHP, is not fully reacted resulting in the presence of Mg in the precipitate. Mg can also be present in MHP due to co-precipitation or as a component of entrained liquor. Additionally, magnesium was identified as a key impurity when recovering nickel as $Ni(OH)_2$ (0.5–12 wt.% Mg) from agro-mined nickel bio-ore [9].

Moreover, the presence of magnesium in nickel solution at a higher concentration can significantly affect the nickel electropolishing process [4], although some studies have shown how magnesium can be tolerated in nickel electrowinning [10]. Due to the need of high purity nickel sulfate and strict magnesium impurity specifications, magnesium must be removed from the system, which can be carried out by precipitation of magnesium fluoride [4, 11, 12].

However, the use of fluoride introduces a risk of contaminating the nickel product and may complicate the water treatment requirements [4, 13]. In acid solutions, fluoride can increase the corrosion rates of the processing equipment [13, 14]. While fluoride is an essential element for human health at lower concentrations (0.4 and 1.0 $mg{\cdot}L^{-1}$) in drinking water, preventing dental diseases [15, 16], continuous consumption of water containing fluoride above 2 $mg{\cdot}L^{-1}$ may contribute to several human health conditions [17–20].

✉ James W. Vaughan
james.vaughan@uq.edu.au

[1] Department of Mining Engineering, Federal University of Minas Gerais, Belo Horizonte 31270-901, Brazil

[2] School of Chemical Engineering, University of Queensland, St Lucia 4072, Australia

Therefore, there are typically strict limits on the discharge of solutions containing fluoride to the environment or to wastewater treatment facilities [21].

To minimize environmental impacts associated with metal production and promote sustainable operations, it is important to consider safe management [22], and recycling of post-consumer waste such as spent LIB [23]. The demand for Li-ion batteries for electric vehicles and other devices has increased significantly, making the recovery of value metals critical [24]. A key challenge in LIB recycling lies in the electrolyte which often contains lithium hexafluorophosphate ($LiPF_6$). Hexafluorophosphate reacts with water or humidity releasing HF into solution in water washing or leaching steps in recycling processes [25].

Fluoride separation technologies are adsorption [26–29], chemical precipitation [30], ion exchange [31, 32], reverse osmosis [33], electrodialysis [34], nanofiltration [35], and electrochemical processes [36] which have been applied in the purification of drinking water or treatment of wastewaters [37]. Among all these techniques, adsorption and ion exchange processes are more effective for the low concentration range of fluoride and are also easy to implement if low cost materials are applied for the adsorption procedure [38–43]. However, the removal of fluoride from concentrated nickel sulfate solution has not been reported in the literature. High purity nickel sulfate is now required in large quantities as a raw material used in the fabrication of rechargeable batteries.

Several fluoride removal materials have been studied and utilized for the fluoride uptake from contaminated waters [39], including zirconium-based materials, which have been the subject of recent investigations due to their high binding affinity towards fluoride [32, 44–47]. Key articles about using zirconium-based materials for fluoride removal are summarized in Table 1.

Another feature that stands out in the use of zirconium compounds for fluoride removal is the possibility of regeneration. Regenerative tests of adsorbents composed of zirconium used in the removal of fluorides were carried out by Blackwell et al. [62], Guo et al. [50]; He and Chen [63]; Hiremath and Theodore [47]; Liao and Shi [60]; Paudyal et al. [55]; Zhang et al. [56] and Tan et al. [42], where NaOH was typically used.

Specifically, HZO has attracted attention due to its relatively large surface area of 148–263 $m^2 \cdot g^{-1}$ [64], high adsorption rate, heat and radiation resistance, free from the

Table 1 Summary of studies using zirconium-based materials for fluoride removal

Materials	Solution source	Operation mode	pH value	Loading capacity ($mg \cdot g^{-1}$)	Ref
Mesoporous carbon modified with hydrated zirconium oxide	Fluoride solution	Batch	5.0	Not reported	[48]
Zirconium-based metal organic frameworks	Fluoride solution	Batch	Not reported	19	[42]
Zirconium oxide coated on activated alumina	Fluoride solution	Batch	5.5	37	[49]
Carbohydrate embedded with hydrous zirconium oxide (HZO) nanoparticles	Synthetic water	Batch and continuous	3.0, 7.0 and 9.0	15	[50]
Zirconium-chitosan/graphene oxide membrane	Fluoride solution	Batch	3.0–11.0	29	[51]
Green algae impregnated with zirconium	Fluoride solution	Batch	2.0–8.0	9.5	[47]
Fe_3O_4 superparamagnetic nanoparticles modified with zirconium oxide	Fluoride solution	Batch	2.5	159	[46]
Hybrid anion exchanger with dispersed zirconium oxide nanoparticles	Fluoride solution	Batch and continuous	5.5	Not reported	[52]
Activated carbon modified with zirconium (IV)	Fluoride solution	Batch	7.0	18	[53]
Polystyrene anion exchanger supported HZO nanoparticles	Synthetic solution, acidic mine drainage	Batch and continuous	7.0 and 3.5	24 and 135	[54]
Granular HZO	Fluoride solution	Batch	4.0 and 7.0	124 and 68	[45]
	Fluoride solution	Continuous	3.0	17	[55]
Zirconium-modified-Na-attapulgite	Fluoride solution	Batch	4.1	19	[56]
Granular zirconium-iron oxide (GZI)	Fluoride solution	Continuous	8.3	0.33	[57]
Zirconium (IV) loaded carboxylated chitosan beads (Zr-CCB)	Fluoride solution	Batch	7.0	4.9	[58]
Zirconium impregnated coconut shell carbon	Fluoride solution	Batch	4.0	6.4	[59]
Zirconium (IV)-impregnated collagen fiber	Fluoride solution	Batch	5.5	41	[60]
Zirconium (IV) complexes of the chelating resins functionalized with amine-N-acetate	Fluoride solution	Batch	5.0	22	[61]
Zirconium oxide microparticulate	Fluoride solution	Batch	4.8	19	[62]

interference of other ions, low solubility in water and good defluorination performance at lower pH value [43, 45, 65]. These characteristics make HZO an attractive adsorbent for the nickel liquor, which has a high concentration of sulfates, low pH value and requires low levels of soluble contaminants in subsequent process stages.

Knowledge of fluoride removal performance is essential to evaluate the feasibility of HZO for this specific application. To evaluate the stable species in the Ni–Zr–F–SO_4–H_2O system, chemical equilibrium modeling using PHREEQC software was carried out. This free software has been extensively used to predict the solid phase formation in aqueous systems and can be useful in the prediction of complexes containing fluorides.

Therefore, this work aims to study the removal of residual fluoride present in concentrated nickel sulfate solution derived from the selective nickel leaching of MHP to separate cobalt and manganese, followed by the removal of magnesium from solution by fluoride precipitation. Guided by chemical-thermodynamic simulations, experiments were performed using a synthetic solution in order to evaluate the performance of previously prepared HZO. Aiming to assess the regenerative capacity of the HZO used in the fluoride removal process in concentrated nickel sulfate solution, regenerations tests were also carried out.

2 Experimental

2.1 Materials

2.1.1 Synthesis of HZO

A zirconium solution of 0.3 mol·L^{-1} was prepared via dissolving the $ZrOCl_2{\cdot}8H_2O$ in distilled water with vigorous stirring. The pH value of the $ZrOCl_2{\cdot}8H_2O$ solution was adjusted to 7.5 using NaOH solution of 1 mol·L^{-1}, while the solution was continuously stirred for 90 min. The precipitated solids were vacuum filtered in a 0.45 µm cellulose acetate membrane, followed by washing with distilled water until the conductivity of the filtrate was lower than 1 mS·cm^{-1}. The solids were collected, dried at 60 °C for 24 h and ground manually to obtain a fine powder [45]. All reagents used in the preparation of HZO and also in the tests were analytical grade. The water content present in the HZO was obtained by heating the samples in a Muffle Furnace (Digital Solid Steel 1200 °C, 7 L) at 350 °C for 5 h and determining the mass loss (molar basis) [64]. The value obtained was compared with $ZrO_2{\cdot}xH_2O$, where x is the amount of water molecules present in the HZO sample. It was confirmed that the HZO used in the experiments were $ZrO{\cdot}2H_2O$ or more chemically accurate, $Zr(OH)_4$.

2.1.2 Synthetic solution preparation

To represent the concentrated nickel sulfate solution obtained from the MHP processing, a synthetic solution containing 100 g·L^{-1} of Ni, 3 g·L^{-1} of Na, 0.36 g·L^{-1} of Mg, 0.1 g·L^{-1} of Ca and 0.32 g·L^{-1} of F was prepared using the following analytical grade reagents: $NiSO_4{\cdot}6H_2O$, Na_2SO_4, $MgSO_4{\cdot}H_2O$, $CaSO_4{\cdot}2H_2O$ and NaF. This solution was used in all experiments unless indicated otherwise.

2.2 Methods and characterization

2.2.1 Chemical analysis and sample characterization

The fluoride concentration in solution was determined by a specific ion electrode thermo scientific orion model 9609BNWP in total ionic strength adjustment buffer II (TISABII) solution prepared by dissolving trans 1,2 diaminocyclohexane N,N,N′N′ tetraacetic acid monohydrate (DCYTA) and NaCl in a mixture of water and acetic acid. The pH value of TISABII solution was raised to 5.5 with NaOH solution [66]. To ensure accurate assays, Ni, Na and Mg were also included in the standards used in the calibration curve in the same amount contained in the synthetic solution, an adaptation of the methodology. The solution was filtered, and the obtained solids were washed with distilled water to remove entrained nickel and then dried at 80 °C. The solids were characterized regarding their functional groups, by Fourier-transform infrared spectroscopy (FTIR, Bruker Alpha, Germany), attenuated total reflectance (ATR), diffuse reflectance accessory (DRIFT). The crystalline solid phases were identified by X-ray diffraction (XRD) with a Bruker D8 Advance XRD (Germany), with a LynxEye detector, and Cu Kα irradiation ($\lambda = 0.15406$ nm) at 40 kV with a scanning speed of 0.05° per second over the 2θ angle range of 5°–40°. The 2014 PDF database from BRUKER was used for reflection identification. The particle size was analyzed using a laser analyzer LS 13 320 XR (Beckman-Coulter, America) which allows determining distribution of particles in the range from 10 nm to 3.5 mm. Aiming at increasing the resolution and enabling reliable measurement of particles, this instrument follows the laser diffraction method with the polarization intensity differential scattering (PIDS) technique, which is based on the phenomenon of different intensities of scattering of vertically and horizontally polarized light. The micro-morphologies were observed using a field emission scanning electron microscopy (FESEM, JOEL 7100F, Japan) with an accelerating voltage of 5 kV and spot size of 30 nm. Scanning electron microscopy (SEM) samples were prepared by dropping a small amount of suspension on the SEM stab and they were air dried. The specific surface area of the material was calculated by N_2 adsorption–desorption isotherms using an American Mike ASAP2020 specific

surface area analyzer. Structural properties of the material were analyzed using a Tristar 2020 apparatus (Micromeritics Instrument Corporation, America). The samples were degassed at 150 °C for 24 h under high vacuum to eliminate adsorbed water from pores of materials prior to nitrogen adsorption at − 196 °C (77 K). Specific surface area was calculated via the multi-point Brunauer–Emmett–Teller (BET) model and the pore size distribution and total pore volume were determined using a density functional theory (DFT) model.

2.2.2 Computational method

Chemical thermodynamic calculations were carried out using PHREEQC software, version 3.4.0.1 2927 (pitzer.dat) to generate the fluoride speciation diagram of the nickel liquor and to simulate the reactions of fluoride removal by zirconium hydroxide.

2.2.3 Fluoride removal experiments

The fluoride removal experiments were carried out in triplicate, in 120 mL polyethylene flasks and a longitudinal shaking system at 70 rpm, 25 ± 3 °C. The solutions were filtered using a 0.45 µm cellulose acetate membrane, then the residual fluoride concentrations were measured. The HZO ($Zr(OH)_4$) was loaded at a fixed weight of 3 g·L^{-1}. The pH value of the suspension was adjusted to the desired value with a 25 vol.% H_2SO_4 solution.

2.2.4 Kinetic and isotherm studies

Kinetic tests were carried out with the same amount of HZO (i.e., 3 g·L^{-1} $Zr(OH)_4$) and at the previously determined pH value where the fluoride removal was maximum (pH = 4). The isotherm curves were constructed using nickel sulfate solution and pure (nickel sulfate free) solutions containing only fluoride by varying the concentration of HZO from 0.25 to 7.0 g·L^{-1} for the tests carried out for 24 h, and the pH value was also adjusted as the requirements. The fluoride loading capacity per mass of HZO was determined by the following Eq. (1).

$$q_t = V(C_0 - C_t)/m \tag{1}$$

where q_t (mg·g^{-1}) is the fluoride loading capacity at time t, V (L) is volume of treated effluent, C_0 (mg·L^{-1}) is the initial concentration of HZO, C_t (mg·L^{-1}) is the concentration of adsorbate at time t and m(g) is the mass of HZO. The kinetic results were evaluated using the kinetic models as depicted in Table 2, q_e (mg·g^{-1}) is the loading capacity at equilibrium and k_1 and k_2 are rate constants (s^{-1}). The isotherms models are shown in Table 3. The general forms of Freundlich, Langmuir, Redlich-Peterson and Sips models were used to evaluate the results in the present work where K_F, K_L, K_{RP}, K_S are distribution coefficients, C_e is the aqueous solution concentration and n, q_m, q_{ms}, a_{RP}, β, m_s are model fitting parameters.

Table 2 Kinetic models applied in the fluoride removal tests using HZO

Model	Equation	Ref
Pseudo-first order	$q_t = q_e(1 - e^{-k_1 t})$	[67]
Pseudo-second order	$q_t = \frac{q_e^2 k_2 t}{1 + q_e k_2 t}$	[67, 68]

Table 3 Isotherm equations of Freundlich, Langmuir, Redlich-Peterson and Sips models

Model	Equation	Ref
Freundlich	$q_e = K_F C_e^{1/n}$	[69]
Langmuir	$q_e = \frac{q_m K_L C_e}{1 + K_L C_e}$	[70]
Redlich-Peterson	$q_e = \frac{K_{RP} C_e}{1 + a_{RP} C_e^{\beta}}$	[71]
Sips	$q_e = \frac{q_{ms} K_s C_e^{ms}}{1 + K_s C_e^{ms}}$	[72]

The software OriginPro8.5 was used to obtain the parameters of the fit of models used in this study. In addition to the correlation coefficient (R^2), the reduced χ^2 value from OriginPro8.5 was used as one of the measures of goodness of fit (Eq. (2)). Where n is the number of data, p is the degree of freedom, y_i is the ith y data, and σ_i is the ith error.

$$\text{Reduced } \chi^2 = \frac{1}{n-p} \sum_{i=1}^{n} \frac{(y_i - f_i)^2}{\sigma_i^2}. \tag{2}$$

2.2.5 HZO fluoride loading and regeneration cycles

Initially 100 mL of nickel sulfate solution containing approximately 1 g·L^{-1} of fluoride and 1 g of HZO were combined. The experiments were carried out in 120 mL polyethylene flasks in a longitudinal shaking system at 70 rpm, 25 ± 3 °C for 24 h. The solids were recovered after filtering through a 0.45 µm cellulose acetate membrane filter and washed with 150 mL of distilled water at pH value of 4 to remove the entrained solution associated with the solid. After that, the HZO solids loaded with fluoride were added to 250 mL of 0.2 mol·L^{-1} NaOH solution and stirred with a paddle stirrer at 240 rpm for 2 h. The solids were filtered and washed with distilled water until the pH value of the wash water approached 8. The solids were dried in an oven at 60 °C for 24 h and used again in the next cycle. In all, 5 cycles of

adsorption and desorption were carried out, and the concentration of residual fluoride in the nickel sulfate solution was measured at the end of each cycle. The experiments were carried out in triplicate.

3 Results and discussion

3.1 Characterization of HZO

The synthesized HZO was characterized by XRD, FESEM (Fig. 1) and N_2 adsorption analyses. The result from the XRD analysis shows that the sample is poorly crystalline or amorphous as there is no characteristic peak can be observed in the pattern (Fig. S1). Similar reports have also been presented in previous articles [57, 73]. The amorphous nature of HZO is considered as an advantage for anion exchange or adsorption reactions as they provide large numbers of active sites associated with a loose structure and large specific surface area [74]. The specific surface area was also measured using the N_2 adsorption–desorption technique. The BET specific surface area was found to be 200 $m^2 \cdot g^{-1}$ (Fig. 2), which is relatively large and in an agreement with the previous work [64]. The morphologies of the dried and ground HZO (Fig. 1) reveals that the dried sample contains irregular shaped broken particles of different sizes, which was formed due to the grinding of the agglomerated dry mass of the HZO. The particle size of the dried and ground HZO were also analyzed using the PIDS technique. Almost around 50 vol.% of the particles were found to be smaller than 50 µm (Fig. 3). The sample was scanned twice, while the second run was performed after sonication. However, there

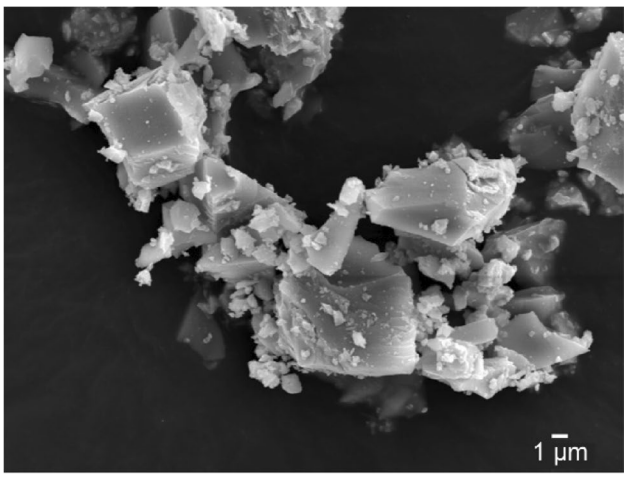

Fig. 1 Micro-morphologies of HZO by FESEM

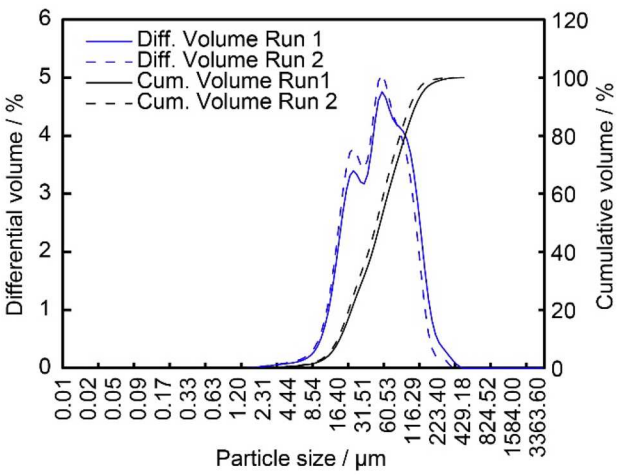

Fig. 3 Particle size distribution of hydrated zirconium oxide

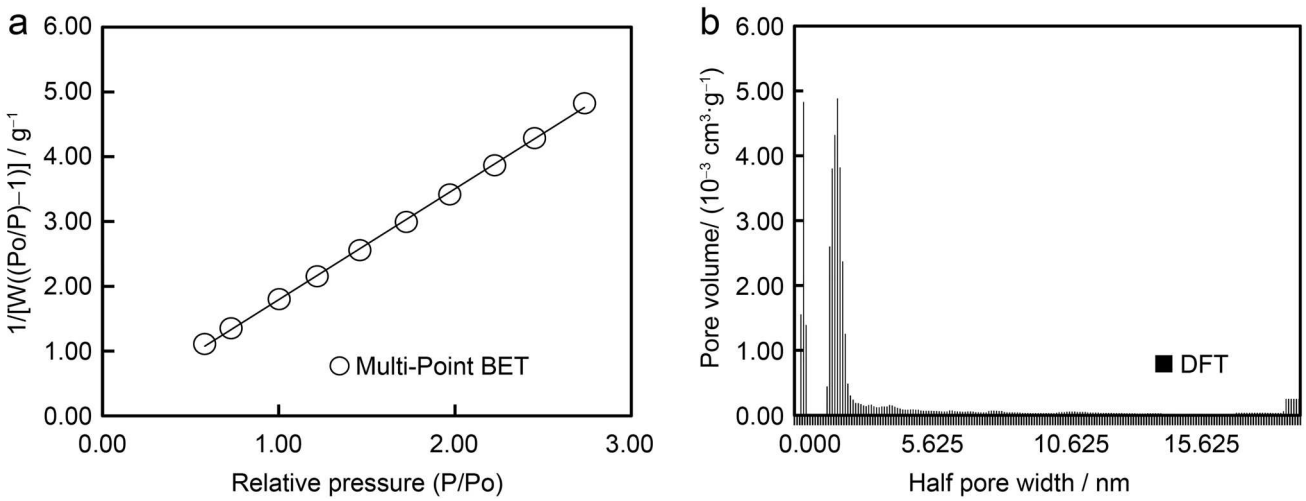

Fig. 2 **a** Specific surface area (Multi-Point BET model) and **b** pore size distribution (DFT)

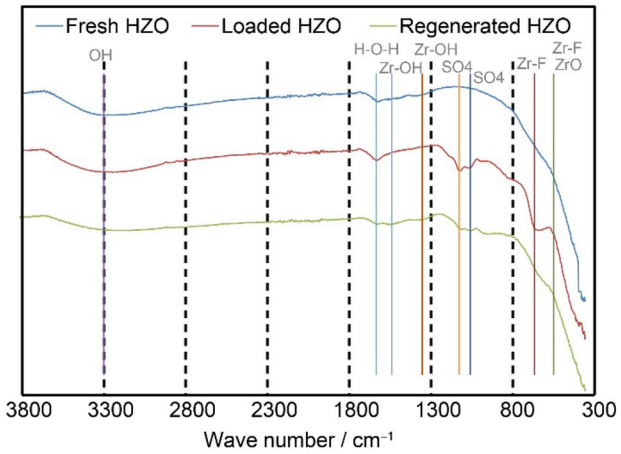

Fig. 4 FTIR spectra of Fresh HZO, HZO after the fluoride removal (Loaded HZO) and HZO after five cycles of adsorption and desorption (Regenerated HZO)

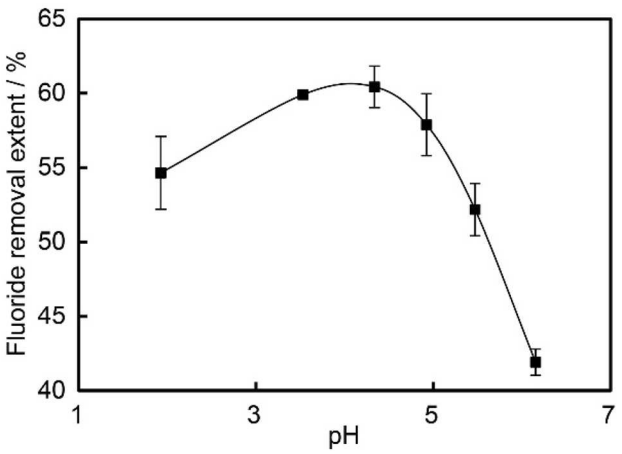

Fig. 5 Fluoride removal extent by HZO as a function of pH. HZO concentration: 3 g·L^{-1}; initial fluoride: 315 mg·L^{-1}; temperature: 25 °C; experimental time: 24 h; stirring rate: 70 rpm; initial pH: 4.5; Solution: Ni 100 g·L^{-1}; Na 3 g·L^{-1}; Mg 0.36 g·L^{-1}; Ca 0.1 g·L^{-1}; F 0.32 g·L^{-1}

was no significant size reduction observed following sonication (Fig. 3, Table S1) which is consistent with the FESEM images. As the dried mass of the HZO was ground manually, the particle size could not be standardized.

The FTIR spectra of Fresh HZO, HZO after the fluoride removal (Loaded HZO) and HZO after five cycles of HZO (Regenerated HZO) loading and regeneration are presented in Fig. 4. The wavenumber at 3300 cm^{-1} can be assigned to the stretching modes of OH band related to the free water [45, 62, 63], and the wavenumber at 1635 cm^{-1} was due to the bending mode of H–O–H band [62, 63, 75]. The 1540 cm^{-1} and 1353 cm^{-1} wavenumbers were assigned to Zr–OH vibration [45] and can only be seen in Fresh HZO and Regenerated HZO samples. This confirms the anion exchange process between OH^- and F^- anions. Other wavenumbers of 1128 cm^{-1} and 1060 cm^{-1} were derived by the sulfate (SO_4) groups [45, 63, 76]. Two other lower frequency peaks at around 667 cm^{-1} and 550 cm^{-1} can be the indication of ZrF_4 formation [54] or terminally linked to Zr–F stretching [77] or Zr–O stretching [70], respectively. Sulfate groups may also be attributed to these two peaks [78]. Nevertheless, at lower frequencies (~ less than 600 cm^{-1}), coupling between various modes of vibration can be observed, which makes it difficult to consider them as pure vibrations [77].

The HZO samples heated at 350 °C for 5 h showed a mass loss of 23.0 ± 0.5%. This value corresponds to the transformation of $ZrO_2{\cdot}2H_2O$ ($Zr(OH)_4$) into ZrO_2 (22.6%), indicating that the HZO has two water molecules.

3.2 Effect of pH

The effects of pH on the fluoride removal efficiency at 25 °C were also studied. Figure 5 shows the F^- removal extent by HZO as a function of pHs of the nickel sulfate solution. The terminal experimental pH value was controlled by addition of sulfuric acid. It is observed that the maximum amount of fluoride removal (60 wt.%) with 3 g·L^{-1} of HZO occurs at pH value close to 4, with a residual concentration of fluoride at 125 ± 4 mg·L^{-1} (pH = 4.3 ± 0.1). As the pH moves away from 4 in both directions, the fluoride removal extent decreases. It should also be noted here that, due to the release of OH^- to the solution, the pH value increases with time while conducting F^- removal. The similar phenomenon has also been demonstrated by Wang et al. [78], while removing fluoride using Zr/calcium sulfate whiskers.

The pH is considered to be a crucial factor in the process of fluoride removal as it can affect the surface charge of the absorbent [78] as well as the fluoride speciation in solution. Dou et al. [45] demonstrated that the efficiency of fluoride removal by adsorption depends on the pH, that affects the electrostatic force existing between the sorbent surface and fluoride species. Lower pH value increases the protonation at the sorbent's surface to generate a higher number of positively charged sites per unit surface area, which in turns enriches the electrostatic attraction force between the positively charged active sites and negative fluoride ions, therefore enhancing the anion exchange reaction with the Zr–OH groups. Contrarily, at higher pH value the absorbent's surface becomes negatively charged and generates repulsion force towards F^- adsorption. The pH value reduction also tends to limit the fluoride removal because of the formation of HF specie in solution, therefore, there is an optimum removal point at pH around 4.0 (Fig. 5). This phenomenon was also observed by Pan et al. [54], who reported the highest capacity for fluoride uptake by polystyrene anion exchanger supported HZO at pH 3.0. Alagumuthu and Rajan [79] pointed out the same optimum pH value of fluoride

adsorption by carbonized ground nutshell impregnated with zirconium oxychloride.

3.3 Fluoride loading kinetics

Figure 6 presents kinetics of fluoride removal by HZO in nickel solution as a removal percentage and per mole of fluoride loaded. There is a rapid fluoride removal of 50 wt.% within the first 7 min, followed by slow removal of fluoride of 60 wt.% at 24 h and 68 wt.% at 72 h. After that, it was observed that the residual fluoride concentration was still decreasing, but more slowly. Thus, after 216 h (9 days) the fluoride removal was 74 wt.%, and after 384 h (16 days) the fluoride removal was 83 wt.%. It should be noted that 16 days is a very long period for industrial processing, therefore, the period of 24 h was adopted for the subsequent tests carried out in this study.

The drop in fluoride concentration may be related to the fact that, when the pH value is kept close to 4 using H_2SO_4, an equilibrium shift occurs causing OH^- anions from the adsorbent surface to be removed and replaced by F^-. Since, during the fluoride removal experiments, the pH increased with time, as previously stated.

Figure 7 presents the fluoride removal kinetics, the adjusted kinetic models of pseudo-first order and pseudo-second order. The model fitting parameters obtained are

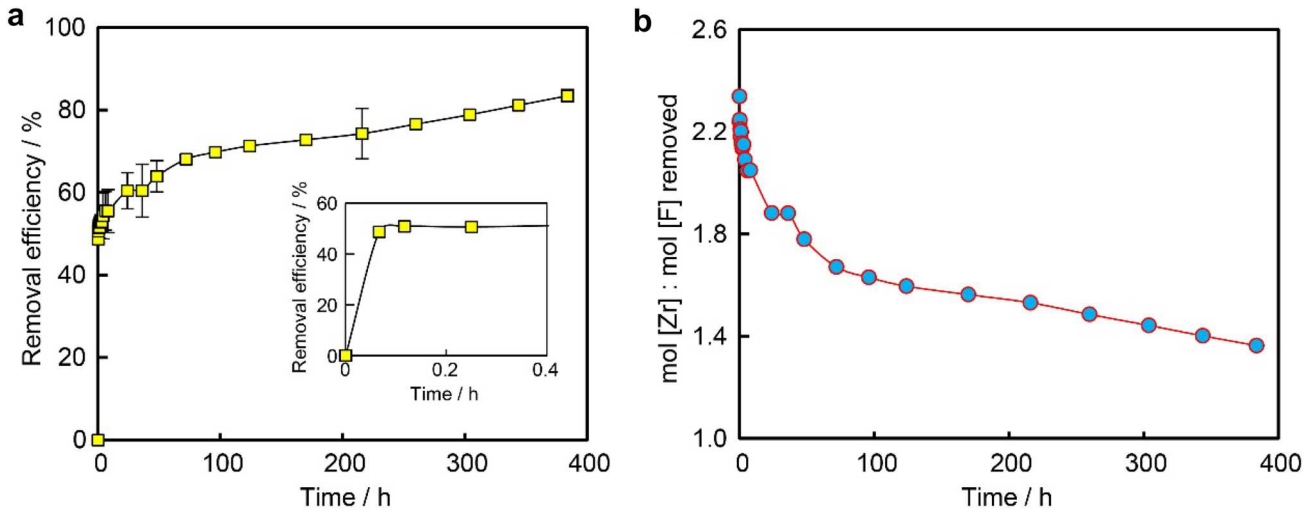

Fig. 6 Kinetics of fluoride removal by HZO in nickel solution as a removal percentage of **a** the initial solution concentration and **b** as a mol fraction ratio of zirconium added to fluoride removed. HZO dose: 3 g·L^{-1}; initial fluoride (measured): 315 mg·L^{-1}; temperature: 25 °C; pH range: 4.3–4.7

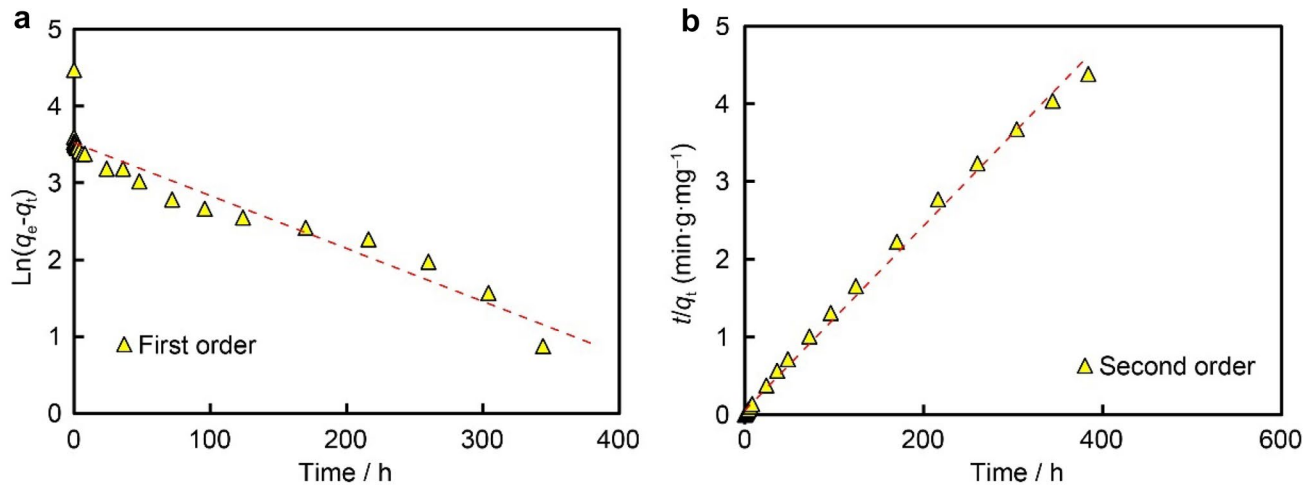

Fig. 7 **a** Pseudo-first order kinetics and **b** pseudo-second order kinetics of fluoride removal by loading onto HZO. HZO dose: 3 g·L^{-1}; initial fluoride (measured): 315 mg·L^{-1}; temperature 25 °C; pH range: 4.3–4.7

Table 4 Kinetic model evaluation for fluoride removal from nickel sulfate solution by HZO

k_1(L · h^{-1})	Pseudo-first-order model			
	k_1 error	q_e(mg·g^{-1})	q_e error	R^2
6.87×10^{-3}	4.65×10^{-4}	33.79	0.56	0.901
k_2(mg · g^{-1} · h^{-1})	Pseudo-second-order model			
	k_2 error	q_e(mg·g^{-1})	q_e error	R^2
2.53×10^{-3}	1.03×10^{-3}	84.16	1.08	0.995

*Solid–liquid ratio: 0.3 g · L^{-1}; temperature: 25 °C; initial fluoride (measured): 315 mg · L^{-1}; pH range 4.3–4.7; Experiment time: 384 h

contained in Table 4 where the quality of the first and second order kinetic model fitting is quantified. The second order model provides a closer fit to the data, however, it appears that there begins to be a negative deviation of the data from the model with extended contacting time.

The results show that the pseudo-second order model fit the experimental data better with an R^2 of 0.995. This result is in accordance with Alagumuthu and Rajan [79], Dou et al. [45], Guo et al. [50] and Tan et al. [42] which also demonstrated that the pseudo-second-order model provided a better fit to the experimental data.

3.4 Adsorption isotherm evaluation

Figure 8a shows fluoride removal behaviour using HZO in synthetic solution of nickel sulfate and in pure solution containing only fluoride in an experimental time of 24 h. The effect of HZO dosage on fluoride removal, exhibit an expected behavior of lower residual fluoride with the increase of the amount of HZO. With 3 g·L^{-1} of HZO, 61 wt.% fluoride is removed (122 mg·L^{-1} of residual fluoride in solution) for the synthetic nickel sulfate solution and a higher removal of 80 wt.% fluoride (65 mg·L^{-1} of residual fluoride) for the pure solution. The presence of nickel sulfate increases the ionic strength of the solution and possibly hinders the interaction between the fluoride and the HZO surface, and there is additional competition for fluoride loading with sulfate. In Fig. 8b, the shape of the curve indicates that there is little interaction between the adsorbent and the fluoride species, especially when using the synthetic solution.

Considering the pseudo-equilibrium time of 24 h, the Langmuir, Freundlich, Redlich–Peterson and Sips models were evaluated to represent the system. Figure 9 shows the curves of the models that obtained the best fits, and the parameters obtained from all applied models are shown in Table 5.

The Freundlich model exhibited a correlation coefficient of 0.929 and this same model was also shown to exhibit a

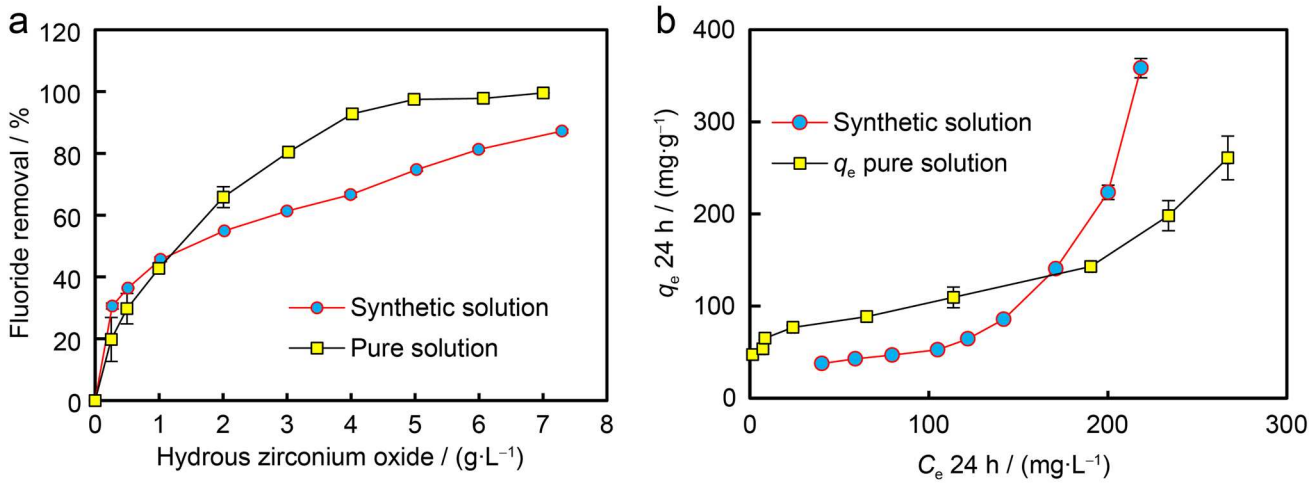

Fig. 8 **a** Fluoride removal as a function of HZO concentration in synthetic solution of nickel sulfate and in pure solution and, **b** as a function of loading capacity (q_e at 24 h contact time) and concentration of fluoride in solution at 24 h. Solid–liquid ratio: 0 to 7.0 g·L^{-1}; temperature: 25 °C; experimental time: 24 h; Synthetic solution (initial fluoride measured: 315 mg·L^{-1}; pH range: 4.3–4.9); pure solution (initial fluoride measured: 333 mg·L^{-1}; pH range: 3.8–5.6)

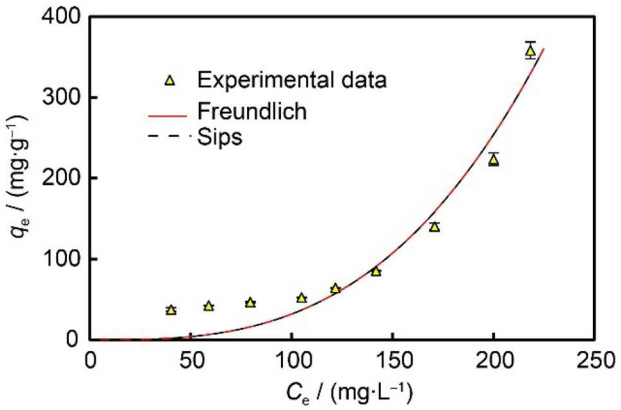

Fig. 9 Data of fitting Freundlich and Sips models on the removal of fluoride by HZO in nickel solution. Solid–liquid ratio: 0–7.0 g·L^{-1}; temperature: 25 °C; initial fluoride (measured): 315 mg·L^{-1}; experiment time: 24 h; pH range: 4.3–4.9

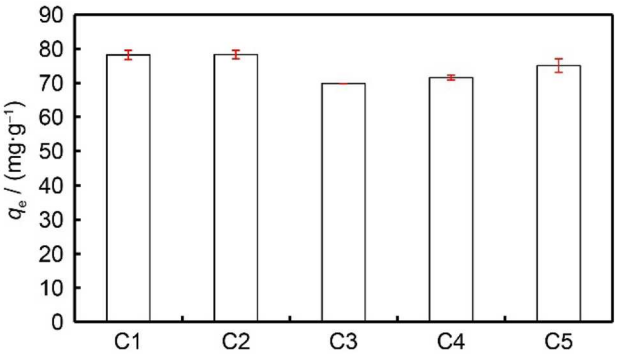

Fig. 10 Fluoride loading as a function of loading/regenerations cycles by HZO in nickel solution. Solid–liquid ratio: 10 g · L^{-1}; temperature: 25 °C; initial fluoride (measured): 986 mg · L^{-1}; experimental time 24 h; pH range: 4.4–5.6

good fit for the data from Dou et al. [45], for the equilibrium concentration in the range of 2–120 mg·L^{-1} of fluoride solution. The Freundlich model describes the adsorption occurring on heterogeneous and amorphous surfaces, which have different adsorption energies and are not restricted to monolayer adsorption [45, 69]. The Sips model, that is an association of Langmuir and Freundlich model [80], presented the second-best fit, at 0.917. This model is derived from the limiting behavior of Langmuir and Freundlich isotherms, characterized by the inclusion of the dimensionless heterogeneity factor, m_s, situated between 0 and 1. When m_s is equal to 1, the Sips equation is reduced to the Langmuir equation, implying a certain degree of homogeneity in the adsorption, which was not observed in the present study [81]. The Langmuir and Redlich–Peterson models presented R^2 of 0.622 and 0.559, therefore, did not fit the experimental data. However, the Freundlich and Sips models are effectively superimposed, and the fit is unsatisfactory in that it deviates significantly negatively from the experimental data as the solution fluoride concentrations become low.

Figure 10 shows the loading capacity obtained from the loading/regeneration cycles by HZO in nickel solution. The results indicate that HZO does not lose its initial loading capacity, even after five cycles of loading and regeneration.

3.5 Fluoride removal mechanism

To understand the anion exchange mechanisms between OH^- and F^- groups, chemical thermodynamic simulations were carried to shed light on the system equilibrium chemical thermodynamics. The data for a crystalline $Zr(OH)_4$ in the PHREEQC database were used for the chemical thermodynamic predictions even though our material was determined to be amorphous according to the XRD results (Fig. S1). The stable ZrO_2 phase was not considered in these simulations as it would not precipitate from aqueous

Table 5 Parameters of data fitting of Langmuir, Freundlich, Redlich-Peterson, Sips and Temkin models on the removal of fluoride by HZO in nickel solution

Langmuir	q_m (mg · g^{-1})	K_L(L · mg^{-1})		$R_{Adj.}^2$	χ^2
	4.264	2.424×10^{-7}		0.622	4482.106
Freundlich	K_F(mg · g^{-1}) (L · mg^{-1})$^{1/n}$	n		$R_{Adj.}^2$	χ^2
	3.455×10^{-5}	0.335		0.929	841.826
Redlich-Peterson	K_{RP}(L · g^{-1})	a_{RP}(L · mg^{-1})	β	$R_{Adj.}^2$	χ^2
	1.034	268.657	− 132.344	0.559	5228.879
Sips	q_{ms} (mg · g^{-1})	K_s(L · mg^{-1})^{ms}	m_s	$R_{Adj.}^2$	X^2
	1.100×10^6	3.038×10^{-11}	2.990	0.917	982.332

Solid–liquid ratio: 0.25–7.0 g · L^{-1}; temperature: 25 °C; initial fluoride (measured): 315 mg · L^{-1}; pH range: 4.3–4.9

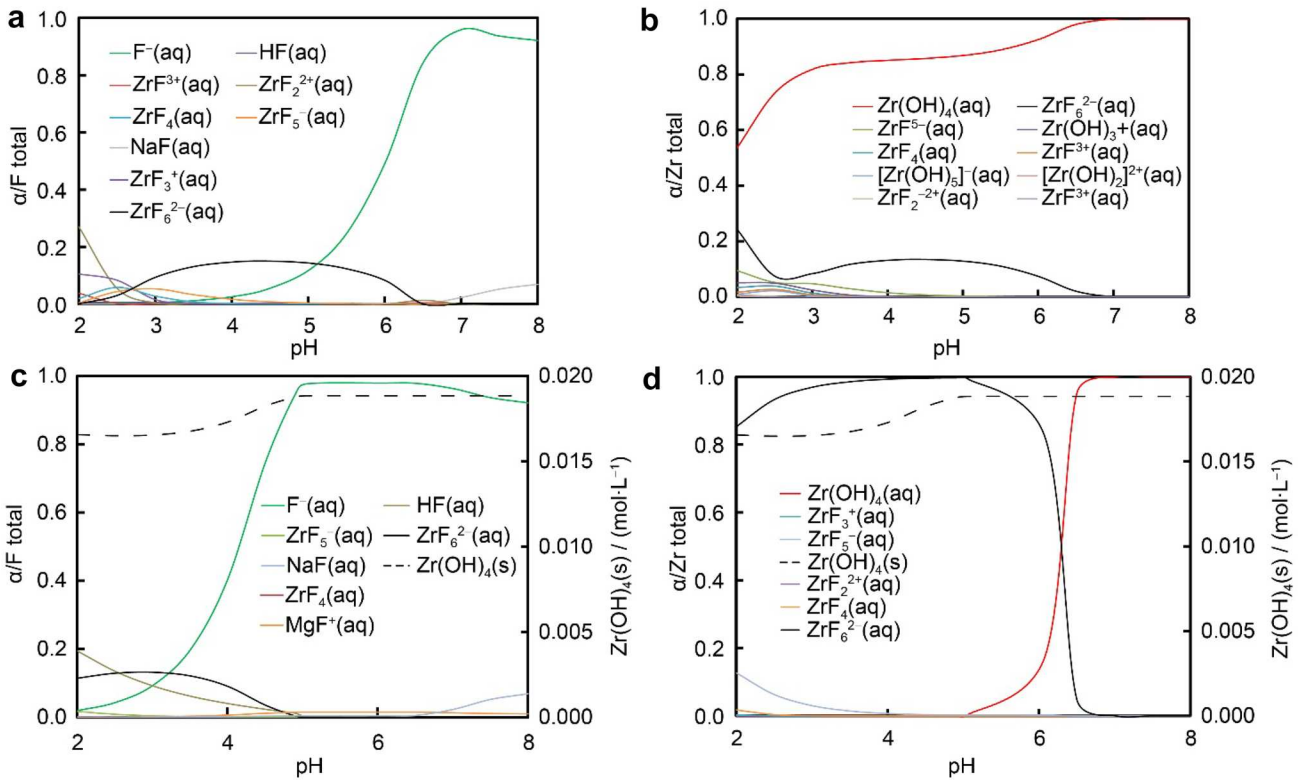

Fig. 11 Speciation-precipitation diagram based on **a** fluoride and **b** zirconium without precipitation of $Zr(OH)_4$ and **c** fluoride and **d** zirconium considering $Zr(OH)_4$ precipitation simulated in PHREEQC software, 3 $g{\cdot}L^{-1}$ HZO, 25 °C; The solution used in the simulations was the composition of the synthetic solution: Ni 100 $g{\cdot}L^{-1}$; Na 3 $g{\cdot}L^{-1}$; Mg 0.36 $g{\cdot}L^{-1}$; Ca 0.1 $g{\cdot}L^{-1}$; F 0.32 $g{\cdot}L^{-1}$

solutions at the temperature used. The anion exchange reactions are believed to be happening at the specific active sites which are not strictly limited by the microstructure of the absorbent [78]. Figure 11 presents the output from the PHREEQC simulation containing the parameters used in the experiments. Figure 11a, b shows the speciation of the solution as a function of total fluoride and total zirconium, respectively, not considering the precipitation of any phase, and Fig. 11c, d shows the speciation of the solution as a function of total fluoride and total zirconium considering the precipitation of $Zr(OH)_4$. Figure 11b represents the aqueous (aq) $Zr(OH)_4$ as the predominant species along with the Zr species in solution. On the other hand, while considering the precipitation of $Zr(OH)_4$(Fig. 11d), the majority of the dissolved zirconium is in the form of ZrF_6^{2-} at pH 4. In Fig. 11a, c, fluoride can be observed in the form of F^- which has a maximum value at pH 7, however, at that pH, the concentration of ZrF_6^{2-} is low. At pH close to 4 we observe that the concentration of ZrF_6^{2-} is higher, that is, there is a possibility of greater number of fluoride-containing complexes being formed.

Alagumuthu and Rajan [79], Dou et al. [45], Pan et al. [54] and Tan et al. [42] suggest that fluoride removal occurs by chemisorption due to the monolayer formation, that is, most likely due to ion exchange of fluoride ions and hydroxyl groups belonging to the adsorbent. The anion-exchange mechanism can be attributed to the isoelectronic and comparable ionic ratio between hydroxyl and fluoride ions, and by the electrostatic interaction between zirconium cation and fluoride ion [42]. In fact, the complex amorphous nature of the hydrated $Zr(OH)_4$ polymorph gives rise to different hydroxyl groups, namely terminal and bridging OH^- groups, along with defects (unsaturated Zr sites) which actively take part in adsorption or anion exchange reactions [82, 83]. Additionally, the unique octahedral nature of the zirconium center increases the accessibility of the exchange site and improves diffusion throughout the framework, which leads to the effective removal of fluoride ions [42] and other probe molecules either via weak hydrogen bonding or covalent bonding at the active sites [83]. While considering the protonation process is the first step of fluoride attack, the terminal OH^- groups ($t-OH^-$) are deemed as the crucial components for chemical interactions within the complex structure of $Zr(OH)_4$ [78]. Wang et al. [78] suggested about two main groups of OH^-, involving of other sub groups based on the different co-ordination environments (i.e., seven-coordinated terminal-OH (7t-OH), eight-coordinated terminal -OH (8t-OH), single bridging -OH (1b-OH) and double bridging -OH

(2b-OH), and demonstrated the fluoride removal process as a combination of protonation and anion exchange within F^- and OH^- groups at specific active sites of the HZO. Acidic conditions facilitated the protonation process and forming low coordinated Zr species which in turns showed stronger affinity towards F^- adsorption.

This process is also justified by the regeneration of the HZO by immersion in a basic solution. However, the ratio of terminal and bridging hydroxyl groups has been reported as 1:3 [78, 82–84] which indicates that only a fraction of OH^- groups (~ 10%) are suitable for the anion exchange or adsorption reaction. As illustrated in Fig. 6b, it is seen that the starting molar ratio of zirconium and fluoride is 1:1 which rises to 2:2 quickly after approximately four minutes of reaction time. However, it was found to then increase more slowly after first few minutes of the reaction (~ 7 min) and finally it rose to 6:9 after 15 days of fluoride removal. Following the Ref. [85] and the experimental results in the present investigation, the fluoride removal mechanism can be described according to the scheme shown in Fig. 12. When fluorides are available in the solution, due to the electron withdrawal capacity of fluoride, there is a possibility of electron accumulation around it, which in turns weakens the Zr–OH bond as well as accelerates the electron charge depletion around the Zr atom. This phenomenon gives rise to the proton attack, formation of low-coordinated Zr atoms and anion exchange within F^- and terminal OH^- groups. Drastic changes in the molar ratio of Zr:F at the beginning of the experiment indicates that the terminal OH^- groups are being exchanged immediately within the first few minutes of the reaction and later the rate decreases due to the lack of availability of terminal OH^- groups, which is also in agreement with the experimental results of the pH of solution that increases over time. Besides, the decreased concentration of available F^- in the solution reduces the driving force for the remaining terminal hydroxyl groups or possibly the bridging OH^- groups to be removed from the structure. It should also be noted here that removal of bridging hydroxyl from the structure is less favorable from a chemical thermodynamic point of view [78].

Based on the data obtained from the simulation (Fig. 11a), the dissolved Zr is predominately ZrF_6^{2-}, ZrF_5^- and ZrF_4 in aqueous solution at around pH 4. According to the FTIR analysis (Fig. 4) and previous reports [42, 45, 78], it is believed that fluoride has been integrated into the solid structure of HZO, preferably via anion exchange with hydroxyl group. Therefore, it can be postulated that the fluoride removal follows the anion exchange mechanism within

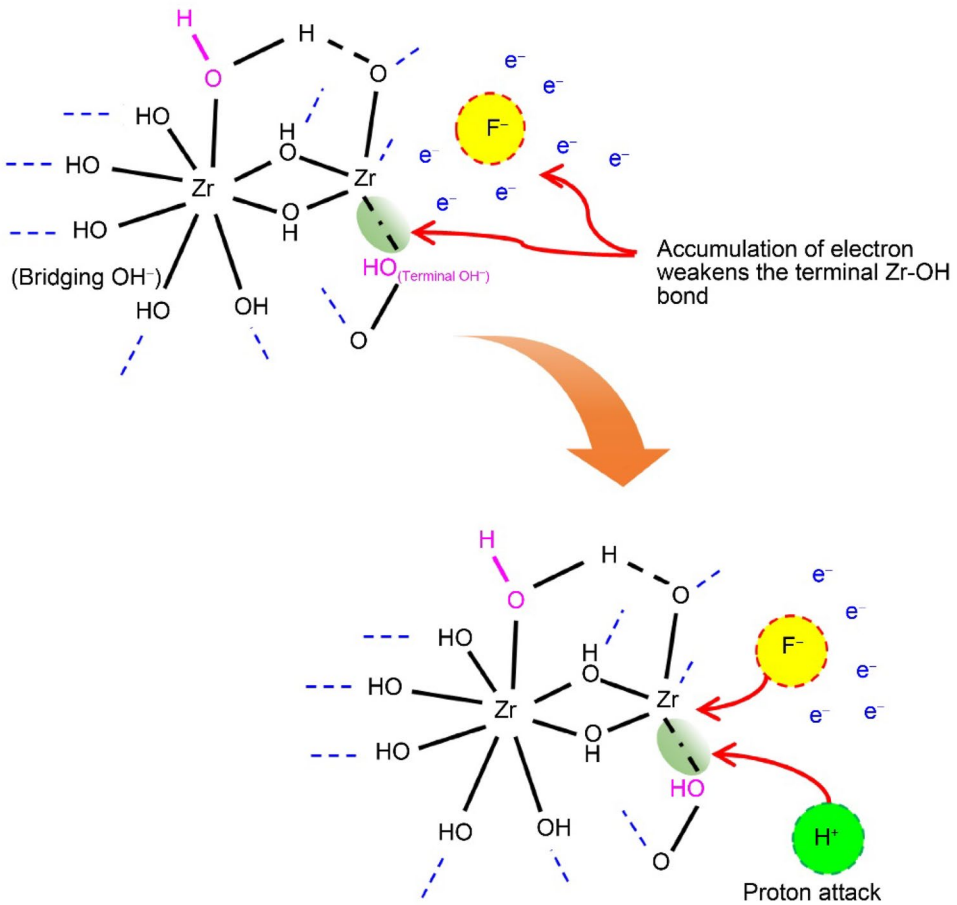

Fig. 12 Schematic representation of the anion exchange mechanism at OH^- sites in amorphous $Zr(OH)_4$ during F removal from solution

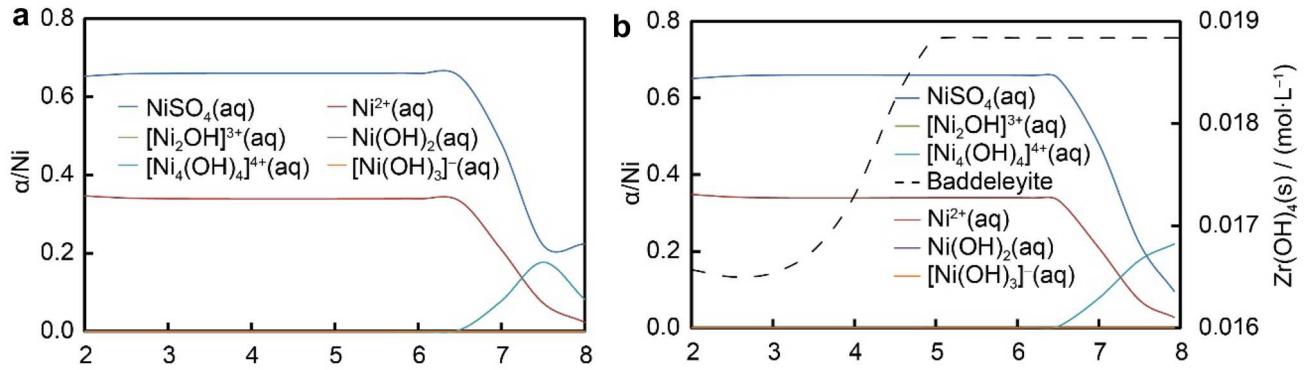

Fig. 13 Speciation diagram based on **a** nickel without precipitation of $Zr(OH)_4$ and **b** considering the $Zr(OH)_4$ precipitation simulated in PHREEQC program. HZO concentration 3 g·L^{-1} (0.019 mol·L^{-1} of $Zr(OH)_4$) in synthetic MHP leach liquor, temperature: 25 °C. PHREEQC considers Zr to precipitates as ZrO_2 as it is more stable, however, experiments demonstrate that Zr is precipitated as $Zr(OH)_4$ in this system. Solution used in the simulation: Ni 100 g·L^{-1}; Na 3 g·L^{-1}; Mg 0.36 g·L^{-1}; Ca 0.1 g·L^{-1}; F 0.32 g·L^{-1}

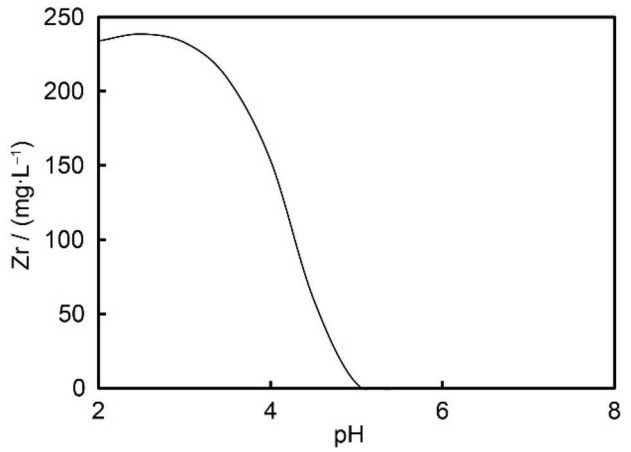

Fig. 14 Soluble zirconium as a function of pH value considering the $Zr(OH)_4$ precipitation from the chemical thermodynamic simulation. HZO concentration of 3 g·L^{-1} (0.019 mol·L^{-1} of $Zr(OH)_4$) in synthetic MHP leach liquor, temperature: 25 °C; Solution used in the simulation: Ni 100 g·L^{-1}; Na 3 g·L^{-1}; Mg 0.36 g·L^{-1}; Ca 0.1 g·L^{-1}; F 0.32 g·L^{-1}

the system and the amount of fluoride adsorbed in relation to the amount of zirconium atoms depends on the number of available sites, as previously discussed. The low crystallinity of the material and the amount of water molecules adhered to the zirconium oxide make it difficult to determine the exact ratio of Zr:F on the structure of the material.

Figure 13 presents the output from the chemical thermodynamic PHREEQC simulation containing the parameters used in the experiments, shows the speciation of the solution as a function of total nickel without precipitation of $Zr(OH)_4$ and considering $Zr(OH)_4$ precipitation. It is observed that nickel is mostly in the form of aqueous $NiSO_4$, followed by Ni^{2+}. It is important to note that nickel does not form fluoride complexes.

Another important factor is to evaluate the residual amount of zirconium in solution that can contaminate the nickel liquor. Figure 14 shows the predicted concentration of soluble zirconium which decreases with increasing pH and, at pH 4.5, the concentration was 60 mg·L^{-1} and below 5 mg·L^{-1} at pH value > 5. In practice, the fate of soluble Zr would also need to be considered as well as the cost of replacement HZO in determining the optimal operating conditions.

4 Conclusions

This study demonstrated the potential for HZO to be used to remove fluoride present in the nickel sulfate liquor, generated after selective leaching of nickel from mixed nickel–cobalt hydroxide that has been subjected to a magnesium fluoride precipitation step. The technology would also find similar application in certain lithium ion battery recycling circuits where fluoride is introduced via hydrolyzed hexafluorophosphate which is a common battery electrolyte component. The fluoride removal kinetics, with 3 g·L^{-1} of HZO, 315 mg·L^{-1} initially, exhibited rapid fluoride removal of 50 wt.% within the first 7 min, followed by slow removal of fluoride of 60 wt.% at 24 h and 68 wt.% at 72 h. After that, it was observed that the residual fluoride concentration was still decreasing, but more slowly. Thus, after 216 h (9 days) the fluoride removal reached 74%, and after 384 h (16 days) the fluoride removal was 83%. The greatest fluoride removal occurs at pH close to 4. Fluoride removal was improved in solutions without nickel sulfate. The Freundlich model fitted the experimental isotherm data best with a correlation coefficient of 0.93, however, the reaction overall is dominated by anion exchange and not physical adsorption. The chemical-thermodynamic simulations indicated the predominance

of ZrF_6^{2-}, ZrF_5^- and ZrF_4 in greater amounts and ZrF_3^+ and ZrF_2^{2+} in smaller amounts in the aqueous solution. The HZO is largely amorphous based on XRD patterns and the presence of Zr–F bonds in the loaded HZO were confirmed by FTIR analysis. The fluoride removal mechanism can be postulated as a complex process involving the protonation process which in result created a low-coordination Zr atom followed by anion exchange between F and OH ions. The HZO also maintained the fluoride loading capacity throughout five cycles of loading and regeneration.

Supplementary Information The online version contains supplementary material available at https://doi.org/10.1007/s42864-023-00241-1.

Acknowledgements The authors acknowledge the financial support from the Brazilian research funding agencies Coordination for the Improvement of Higher Education Personnel (CAPES) for the post-doctoral scholarship, research fellow National Council for Scientific and Technological Development (CNPq - Process 308044/2018-5) and Minas Gerais State Agency for Research and Development (FAPEMIG). The authors are also thankful to the financial support from the University of Queensland Research Stimulus Allocation 2 (Fellowships) scheme for the year of 2021 for awarding a post-doctoral fellowship.

Declarations

Conflict of interest The authors declare no conflict of interest.

Data availability The data generated during and/or analyzed in this article are available from the corresponding author on reasonable request.

References

1. Byrne K, Hawker W, Vaughan J. Effect of key parameters on the selective acid leach of nickel from mixed nickel–cobalt hydroxide. In: AIP conference proceedings. West Java: Indonesia; 2017. p. 136.
2. Farrokhpay S, Filippov L. Challenges in processing nickel laterite ores by flotation. Int J Miner Process. 2016;151:59. https://doi.org/10.1016/j.minpro.2016.04.007.
3. Komnitsas K, Petrakis E, Bartzas G, Karmali V. Column leaching of low-grade saprolitic laterites and valorization of leaching residues. Sci Total Environ. 2019;665:347. https://doi.org/10.1016/j.scitotenv.2019.01.381.
4. Zhaowu Z, Jian Z, Aifei Y, Hui S, Lina W, Tao Q. Magnesium removal from concentrated nickel solution by solvent extraction using Cyanex 272. Int J Miner Process Extr Metall. 2019;4(2):36. https://doi.org/10.11648/j.ijmpem.20190402.11.
5. Dry M, Vaughan J, Hawker W. Environmental evaluation of making nickel sulphate. In: ALTA 2019 nickel–cobalt–copper conference. Perth; 2019. 136.
6. Harvey R, Hannah R, Vaughan J. Selective precipitation of mixed nickel–cobalt hydroxide. Hydrometallurgy. 2011;105(3–4):222. https://doi.org/10.1016/j.hydromet.2010.10.003.
7. Ichlas ZT, Mubarok MZ, Magnalita A, Vaughan J, Sugiarto AT. Processing mixed nickel–cobalt hydroxide precipitate by sulfuric acid leaching followed by selective oxidative precipitation of cobalt and manganese. Hydrometallurgy. 2020;191:105185. https://doi.org/10.1016/j.hydromet.2019.105185.
8. Wang LY, Lee MS. Separation of Co(II) and Ni(II) from chloride leach solution of nickel laterite ore by solvent extraction with Cyanex 301. Int J Miner Process. 2017;166:45. https://doi.org/10.1016/j.minpro.2017.07.004.
9. Vaughan J, Riggio J, Chen J, Peng H, Harris HH, van der Ent A. Characterisation and hydrometallurgical processing of nickel from tropical agromined bio-ore. Hydrometallurgy. 2017;169:346. https://doi.org/10.1016/j.hydromet.2017.01.012.
10. Tripathy BC, Das SC, Singh P, Hefter GT, Muir DM. Effect of Mg^{2+}, Li^+, Na^+ and K^+ on the electrocrystallization of nickel from aqueous sulfate solutions containing boric acid. J Appl Electrochem. 2001;31(5):573. https://doi.org/10.1023/A:1017585726321.
11. Booster JL, Van Sandwijk A, Reuter MA. Magnesium removal in the electrolytic zinc industry. Miner Eng. 2000;13(5):517. https://doi.org/10.1016/S0892-6875(00)00032-7.
12. Zhang X, Laubie B, Houzelot V, Plasari E, Echevarria G, Simonnot MO. Increasing purity of ammonium nickel sulfate hexahydrate and production sustainability in a nickel phytomining process. Chem Eng Res Des. 2016;106:26. https://doi.org/10.1016/j.cherd.2015.12.009.
13. Parsonage D, Singh P, Nikoloski AN. Adverse effects of fluoride on hydrometallurgical operations. Miner Process Extr Metall Rev. 2013;35(1):44. https://doi.org/10.1080/08827508.2012.695306.
14. Suzuki I, Lee D, Mackay B, Harahuc L, Oh JK. Effect of various ions, pH, and osmotic pressure on oxidation of elemental sulfur by Thiobacillus thiooxidans. Appl Environ Microbiol. 1999;65(11):5163. https://doi.org/10.1128/AEM.65.11.5163-5168.1999.
15. Ghorai S, Pant KK. Investigations on the column performance of fluoride adsorption by activated alumina in a fixed-bed. Chem Eng J. 2004;98(1–2):165. https://doi.org/10.1016/j.cej.2003.07.003.
16. WHO. Guidelines for drinking-water quality. 2nd ed. Geneva: World Health Organization; 1996.
17. Harrison PTC. Fluoride in water: a UK perspective. J Fluor Chem. 2005;126(11–12):1448. https://doi.org/10.1016/j.jfluchem.2005.09.009.
18. Nur T, Loganathan P, Nguyen TC, Vigneswaran S, Singh G, Kandasamy J. Batch and column adsorption and desorption of fluoride using hydrous ferric oxide: solution chemistry and modeling. Chem Eng J. 2014;247:93. https://doi.org/10.1016/j.cej.2014.03.009.
19. Tripathy SS, Bersillon JL, Gopal K. Removal of fluoride from drinking water by adsorption onto alum-impregnated activated alumina. Sep Purif Technol. 2006;50(3):310. https://doi.org/10.1016/j.seppur.2005.11.036.
20. Xiong X, Liu J, He W, Xia T, He P, Chen X, Yang K, Wang A. Dose-effect relationship between drinking water fluoride levels and damage to liver and kidney functions in children. Environ Res. 2007;103(1):112. https://doi.org/10.1016/j.envres.2006.05.008.
21. Nationnal Environment Council. CONAMA Resolution 430/11. 2011. https://www.braziliannr.com/brazilian-environmental-legislation/conama-resolution-43011/.

22. Hao M, Liu Y, Wu W, Wang S, Yang X, Chen Z, Tang Z, Huang Q, Wang S, Yang H, Wang X. Advanced porous adsorbents for radionuclides elimination. EnergyChem. 2023;5(4):100101. https://doi.org/10.1016/j.enchem.2023.100101.
23. Zheng Y, Song W, Mo WT, Zhou L, Liu JW. Lithium fluoride recovery from cathode material of spent lithium-ion battery. RSC Adv. 2018;8(16):8990. https://doi.org/10.1039/c8ra00061a.
24. Botelho Junior AB, Stopic S, Friedrich B, Tenório JAS, Espinosa DCR. Cobalt recovery from Li-ion battery recycling: a critical review. Metals. 2021;11(12):1999. https://doi.org/10.3390/met11121999.
25. Larsson F, Andersson P, Blomqvist P, Mellander BE. Toxic fluoride gas emissions from lithium-ion battery fires. Sci Rep. 2017;7(1):10018. https://doi.org/10.1038/s41598-017-09784-z.
26. Gupta AK, Deva D, Sharma A, Verma N. Adsorptive removal of fluoride by micro-nanohierarchical web of activated carbon fibers. Ind Eng Chem Res. 2009;48(21):9697. https://doi.org/10.1021/ie801688k.
27. Jeyaseelan A, Viswanathan N. Investigation of hydroxyapatite-entrenched cerium organic frameworks incorporating biopolymeric beads for efficient fluoride removal. Ind Eng Chem Res. 2022;61(23):7911. https://doi.org/10.1021/acs.iecr.2c00487.
28. Medellin-Castillo NA, Leyva-Ramos R, Ocampo-Perez R, de la Cruz RFG, Aragon-Pina A, Martinez-Rosales JM, Guerrero-Coronado RM, Fuentes-Rubio L. Adsorption of fluoride from water solution on bone char. Ind Eng Chem Res. 2007;46(26):9205. https://doi.org/10.1021/ie070023n.
29. Nigri EM, Bhatnagar A, Rocha SDF. Thermal regeneration process of bone char used in the fluoride removal from aqueous solution. J Clean Prod. 2017;142:3558. https://doi.org/10.1016/j.jclepro.2016.10.112.
30. Benefield LD, Judkins JF, Weand BL. Process chemistry for water and wastewater treatment. Englewood Cliffs: Prentice-Hall Englewood Cliffs; 1981.
31. Kunin R. Ion exchange resins. 2nd ed. Malabar: R.E. Krieger; 1990.
32. Swain SK, Mishra S, Sharma P, Patnaik T, Singh VK, Jha U, Patel RK, Dey RK. Development of a new inorganic-organic hybrid ion-exchanger of zirconium(IV)-propanolamine for efficient removal of fluoride from drinking water. Ind Eng Chem Res. 2010;49(20):9846. https://doi.org/10.1021/ie1012536.
33. Colla V, Branca TA, Rosito F, Lucca C, Vivas BP, Delmiro VM. Sustainable reverse osmosis application for wastewater treatment in the steel industry. J Clean Prod. 2016;130:103. https://doi.org/10.1016/j.jclepro.2015.09.025.
34. Gwala P, Andey S, Mhaisalkar V, Labhasetwar P, Pimpalkar S, Kshirsagar C. Lab scale study on electrocoagulation defluoridation process optimization along with aluminium leaching in the process and comparison with full scale plant operation. Water Sci Technol. 2011;63(12):2788. https://doi.org/10.2166/wst.2011.475.
35. Simons R. Trace-element removal from ash dam waters by nanofiltration and diffusion dialysis. Desalination. 1993;89(3):325. https://doi.org/10.1016/0011-9164(93)80145-D.
36. Drouiche N, Ghaffour N, Aoudj S, Hecini M, Ouslimane T. Fluoride removal from photovoltaic wastewater by aluminium electrocoagulation and characteristics of products. Chem Eng Trans. 2009;17:1651. https://doi.org/10.3303/Cet0917276.
37. Agarwal M, Rai K, Shrivastav R, Dass S. Deflouridation of water using amended clay. J Clean Prod. 2003;11(4):439. https://doi.org/10.1016/S0959-6526(02)00065-3.
38. Nigri EM, Cechinel MA, Mayer DA, Mazur LP, Loureiro JM, Rocha SD, Vilar VJ. Cow bones char as a green sorbent for fluorides removal from aqueous solutions: batch and fixed-bed studies. Environ Sci Pollut Res Int. 2017;24(3):2364. https://doi.org/10.1007/s11356-016-7816-5.
39. Bhatnagar A, Kumar E, Sillanpaa M. Fluoride removal from water by adsorption—a review. Chem Eng J. 2011;171(3):811. https://doi.org/10.1016/j.cej.2011.05.028.
40. Vocciante M, Trofa M, Rodriguez-Estupinan P, Giraldo L, D'Auria T, Moreno-Pirajan JC, Erto A. A rigorous procedure for the design of adsorption units for the removal of cadmium and nickel from process wastewaters. J Clean Prod. 2014;77:35. https://doi.org/10.1016/j.jclepro.2013.12.001.
41. Meenakshi, Maheshwari RC. Fluoride in drinking water and its removal. J Hazard Mater. 2006;137(1):456. https://doi.org/10.1016/j.jhazmat.2006.02.024.
42. Tan TL, Krusnamurthy PA, Nakajima H, Rashid SA. Adsorptive, kinetics and regeneration studies of fluoride removal from water using zirconium-based metal organic frameworks. RSC Adv. 2020;10(32):18740. https://doi.org/10.1039/d0ra01268h.
43. He JG, Li Y, Xue XX, Ru HQ, Huang XW, Yang H. Removal of fluoride from fluoride-Bering cerium sulfate solution by hydrous zirconium oxide. Metalurgija. 2014;53(2):183. https://doaj.org/article/a572ad9d14fd40f983a512fb7e52ff67.
44. Viswanathan N, Meenakshi S. Effect of metal ion loaded in a resin towards fluoride retention. J Fluor Chem. 2008;129(7):645. https://doi.org/10.1016/j.jfluchem.2008.05.007.
45. Dou XM, Mohan D, Pittman CU, Yang S. Remediating fluoride from water using hydrous zirconium oxide. Chem Eng J. 2012;198:236. https://doi.org/10.1016/j.cej.2012.05.084.
46. Riahi F, Bagherzadeh M, Hadizadeh Z. Modification of Fe_3O_4 superparamagnetic nanoparticles with zirconium oxide; preparation, characterization and its application toward fluoride removal. RSC Adv. 2015;5(88):72058. https://doi.org/10.1039/c5ra14833b.
47. Hiremath PG, Theodore T. Modelling of fluoride sorption from aqueous solution using green algae impregnated with zirconium by response surface methodology. Adsorpt Sci Technol. 2016;35(1–2):194. https://doi.org/10.1177/0263617416674014.
48. Takada T. Removal of F-from water using templated mesoporous carbon modified with hydrated zirconium oxide. C J Carbon Res. 2020;6(1):13. https://doi.org/10.3390/c6010013.
49. Yavari R. Investigation and comparison of fluoride adsorption behavior on a hybrid material containing zirconium dioxide coated on γ-alumina (60 and 90) and their initial precursor in aqueous solution. J Water Environ Nanotechnol. 2019;4(4):321. https://doi.org/10.22090/jwent.2019.04.006.
50. Guo Y, Xu X, Shang Y, Gao B. Removal of fluoride by carbohydrate-based material embedded with hydrous zirconium oxide nanoparticles. Environ Sci Pollut Res Int. 2018;25(28):27982. https://doi.org/10.1007/s11356-018-2851-z.
51. Zhang J, Chen N, Su PY, Li M, Feng CP. Fluoride removal from aqueous solution by zirconium-chitosan/graphene oxide membrane. React Funct Polym. 2017;114:127. https://doi.org/10.1016/j.reactfunctpolym.2017.03.008.
52. Padungthon S, Li JZ, German M, SenGupta AK. Hybrid anion exchanger with dispersed zirconium oxide nanoparticles: a durable and reusable fluoride-selective sorbent. Environ Eng Sci. 2014;31(7):360. https://doi.org/10.1089/ees.2013.0412.
53. Velazquez-Jimenez LH, Hurt RH, Matos J, Rangel-Mendez JR. Zirconium-carbon hybrid sorbent for removal of fluoride from water: oxalic acid mediated Zr(IV) assembly and adsorption mechanism. Environ Sci Technol. 2014;48(2):1166. https://doi.org/10.1021/es403929b.
54. Pan B, Xu J, Wu B, Li Z, Liu X. Enhanced removal of fluoride by polystyrene anion exchanger supported hydrous zirconium oxide nanoparticles. Environ Sci Technol. 2013;47(16):9347. https://doi.org/10.1021/es401710q.
55. Paudyal H, Pangeni B, Inoue K, Kawakita H, Ohto K, Alam S. Removal of fluoride from aqueous solution by using porous resins containing hydrated oxide of cerium(IV) and zirconium(IV).

J Chem Eng Jpn. 2012;45(5):331. https://doi.org/10.1252/jcej.11we181.
56. Zhang G, He ZL, Xu W. A low-cost and high efficient zirconium-modified-Na-attapulgite adsorbent for fluoride removal from aqueous solutions. Chem Eng J. 2012;183:315. https://doi.org/10.1016/j.cej.2011.12.085.
57. Dou X, Zhang Y, Wang H, Wang T, Wang Y. Performance of granular zirconium-iron oxide in the removal of fluoride from drinking water. Water Res. 2011;45(12):3571. https://doi.org/10.1016/j.watres.2011.04.002.
58. Viswanathan N, Meenakshi S. Synthesis of Zr(IV) entrapped chitosan polymeric matrix for selective fluoride sorption. Colloids Surf B Biointerfaces. 2009;72(1):88. https://doi.org/10.1016/j.colsurfb.2009.03.021.
59. Sathish RS, Raju NSR, Raju GS, Rao GN, Kumar KA, Janardhana C. Equilibrium and kinetic studies for fluoride adsorption from water on zirconium impregnated coconut shell carbon. Sep Sci Technol. 2007;42(4):769. https://doi.org/10.1080/01496390601070067.
60. Liao XP, Shi B. Adsorption of fluoride on zirconium(IV)-impregnated collagen fiber. Environ Sci Technol. 2005;39(12):4628. https://doi.org/10.1021/es0479944.
61. Tanaka DAP, Kerketta S, Tanco MAL, Yokoyama T, Suzuki TM. Adsorption of fluoride ion on the zirconium(IV) complexes of the chelating resins functionalized with amine-N-acetate ligands. Sep Sci Technol. 2002;37(4):877. https://doi.org/10.1081/ss-120002221.
62. Blackwell JA, Carr PW. Study of the fluoride adsorption characteristics of porous microparticulate zirconium-oxide. J Chromatogr. 1991;549(1–2):43. https://doi.org/10.1016/S0021-9673(00)91417-1.
63. He J, Chen JP. A zirconium-based nanoparticle: essential factors for sustainable application in treatment of fluoride containing water. J Colloid Interface Sci. 2014;416:227. https://doi.org/10.1016/j.jcis.2013.10.032.
64. da Silva GLJP, da Silva MLCP, Caetano T. Preparation and characterization of hydrous zirconium oxide formed by homogeneous precipitation. Mater Res. 2002;5(2):149. https://doi.org/10.1590/s1516-14392002000200011.
65. Chitrakar R, Tezuka S, Sonoda A, Sakane K, Ooi K, Hirotsu T. Selective adsorption of phosphate from seawater and wastewater by amorphous zirconium hydroxide. J Colloid Interface Sci. 2006;297(2):426. https://doi.org/10.1016/j.jcis.2005.11.011.
66. Rice EW, Bridgewater L. Standard methods for the examination of water and wastewater. 22nd ed. Washington: American Public Health Association, 2012.
67. Ho YS. Review of second-order models for adsorption systems. J Hazard Mater. 2006;136(3):681. https://doi.org/10.1016/j.jhazmat.2005.12.043.
68. Lagergren SK. About the theory of so-called adsorption of soluble substances. Proc R Swedish Acad Sci. 1898;24:1. https://www.scinapse.io/papers/2212997086.
69. Freundlich H. Über die Adsorption in Lösungen. Z Phys Chem. 1907;57U(1):385. https://doi.org/10.1515/zpch-1907-5723.
70. Langmuir I. The constitution and fundamental properties of solids and liquids part I solids. J Am Chem Soc. 1916;38(11):2221. https://doi.org/10.1021/ja02268a002.
71. Redlich O, Peterson DL. A useful adsorption isotherm. J Phys Chem. 1959;63(6):1024. https://doi.org/10.1021/j150576a611.
72. Sips R. On the structure of a catalyst surface. J Chem Phys. 1948;16(5):490. https://doi.org/10.1063/1.1746922.
73. Chen PH, Zhang WB, Li ML, Ai P, Tian L, Jiang HL. Facile synthesis of magnetic La–Zr composite as high effective adsorbent for fluoride removal. RSC Adv. 2016;6(42):35859. https://doi.org/10.1039/c5ra27929a.
74. Cai HM, Chen GJ, Peng CY, Xu LY, Zhang ZZ, Ke F, Wan XC. Enhanced fluoride removal by loading Al/Zr onto carboxymethyl starch sodium: synergistic interactions between Al and Zr. RSC Adv. 2015;5(123):101819. https://doi.org/10.1039/c5ra18167d.
75. Cao CY, Li P, Qu J, Dou ZF, Yan WS, Zhu JF, Wu ZY, Song WG. High adsorption capacity and the key role of carbonate groups for heavy metal ion removal by basic aluminum carbonate porous nanospheres. J Mater Chem. 2012;22(37):19898. https://doi.org/10.1039/c2jm34138g.
76. Mo M, Zeng Q, Li M. Study of the fluorine adsorption onto zirconium oxide deposited strong alkaline anion exchange fiber. J Appl Polym Sci. 2018;135(7):45855. https://doi.org/10.1002/app.45855.
77. Jere GV, Santhamma MT. Ir and laser Raman studies on peroxo fluoro species of zirconium. Inorg Chim Acta. 1977;24(1):57. https://doi.org/10.1016/S0020-1693(00)93851-9.
78. Wang L, Huang Y, Zhou D, Chen XF, Zhao HR, Li X, Hughes SS, Zhang PC, He P, Zhang GR, Cheng X, Zhang RX. Efficient removal of fluoride from neutral wastewater by green synthesized Zr/calcium sulfate whiskers: an experimental and theoretical study. Colloids Surf A Physicochem Eng Asp. 2021;630:127587. https://doi.org/10.1016/j.colsurfa.2021.127587.
79. Alagumuthu G, Rajan M. Kinetic and equilibrium studies on fluoride removal by zirconium (Iv)-impregnated groundnut shell carbon. Hemijska Industrija. 2010;64(4):295. https://doi.org/10.2298/Hemind100307017a.
80. Drouiche N, Aoudj S, Hecini M, Ghaffour N, Lounici H, Mameri N. Study on the treatment of photovoltaic wastewater using electrocoagulation: fluoride removal with aluminium electrodes-characteristics of products. J Hazard Mater. 2009;169(1–3):65. https://doi.org/10.1016/j.jhazmat.2009.03.073.
81. Ghosh D, Medhi CR, Purkait MK. Treatment of fluoride containing drinking water by electrocoagulation using monopolar and bipolar electrode connections. Chemosphere. 2008;73(9):1393. https://doi.org/10.1016/j.chemosphere.2008.08.041.
82. Ouyang F, Nakayama A, Tabada K, Suzuki E. Infrared study of a novel acid–base site on ZrO_2 by adsorbed probe molecules. I. Pyridine, carbon dioxide, and formic acid adsorption. J Phys Chem B. 2000;104(9):2012. https://doi.org/10.1021/jp992970i.
83. McEntee M, Peterson GW, Balboa A, Iordanov I, Balow RB, Pehrsson PE. Surface chemistry of sulfur dioxide on $Zr(OH)_4$ powder: the role of water. J Phys Chem C. 2019;123(28):17205. https://doi.org/10.1021/acs.jpcc.9b00790.
84. Southon PD, Bartlett JR, Woolfrey JL, Ben-Nissan B. Formation and characterization of an aqueous zirconium hydroxide colloid. Chem Mater. 2002;14(10):4313. https://doi.org/10.1021/cm0211913.
85. Cong RH, Wang Y, Kang L, Zhou ZY, Lin ZH, Yang T. An outstanding second-harmonic generation material BiB_2O_4F: exploiting the electron-withdrawing ability of fluorine. Inorg Chem Front. 2015;2(2):170. https://doi.org/10.1039/c4qi00192c.